Supplementary information:
High harmonic generation reflecting the sub-cycle evolution of the Mott transition under a mid-infrared electric field

Ryohei Ikeda[1], Yuta Murakami[2,3], Daiki Sakai[1], Tatsuya Miyamoto[1,4], Toshimitsu Ito[5], Hiroshi Okamoto[1]

[1]*Department of Advanced Materials Science, University of Tokyo, Chiba 277-8561, Japan*
[2]*Institute for Materials Research, Tohoku University, Sendai 980-8577, Japan*
[3]*Center for Emergent Matter Science, RIKEN, Wako, Saitama 351-0198, Japan*
[4]*Department of Engineering, Nagoya Institute of Technology, Nagoya, 466-8555, Japan*
[5]*National Institute of Advanced Industrial Science and Technology, Tsukuba 305-8565, Japan*

Table of contents

S1 Evaluation of temporal width and maximum electric field of MIR pump pulses
S2 Polarisation dependence of HH spectra
S3 Fitting analysis of transient reflectivity changes induced by MIR pump pulses
S4 Evaluation of the carrier density generated by MIR pump pulses
S5 Supplementary data of DMFT simulations

S1 Evaluation of temporal width and maximum electric field of MIR pump pulses

Figures S1(a) and (b) show the spectra of the MIR pulses used for pump-probe reflectivity (PPR) and HHG measurements, respectively. The central photon energies of the MIR pulses were 0.264 and 0.263 eV for the PPR and HHG measurements, respectively, which are almost the same. The full widths at half maximum (FWHM) of the MIR pulses were 24 meV and 22 meV for the PPR and HHG measurements, respectively.

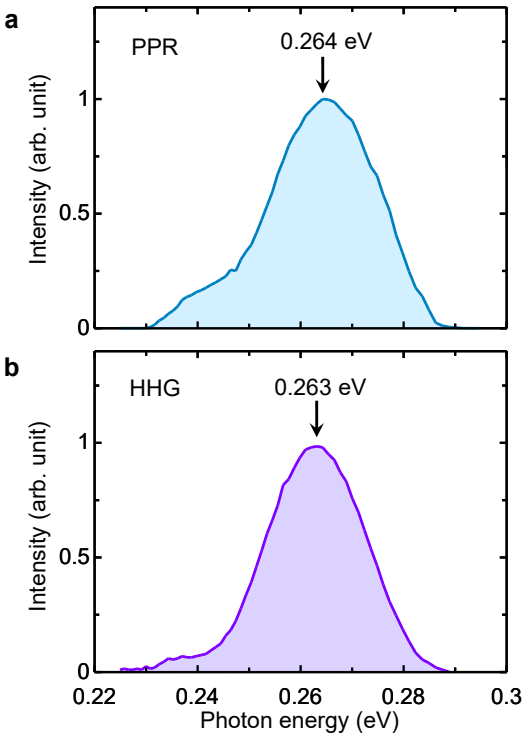

Fig. S1 | Spectra of MIR pulses. (**a**) PPR and (**b**) HHG measurements.

Although estimating the temporal width of an MIR pulse is generally difficult, it is possible by using the time characteristic of the reflectivity change $-\Delta R/R(t)$ under weak excitation (Fig. 3d), which can be regarded as a coherent response, obtained from PPR measurements. As a typical example of such a coherent response, Fig. S2(a) shows the time characteristic of $-\Delta R/R(t)$ for $E_{\mathrm{MIR}} = 3.0\,\mathrm{MV/cm}$. Next, we explain this response. In 1D Mott insulators, a one-photon-allowed excitonic state with odd-parity, $|\varphi_{\mathrm{o}}\rangle$, is the lowest excited state and a one-photon-forbidden excitonic state with even-parity, $|\varphi_{\mathrm{e}}\rangle$, is located just above $|\varphi_{\mathrm{o}}\rangle$[1-4], as shown on the left side of Fig. S2(b). When

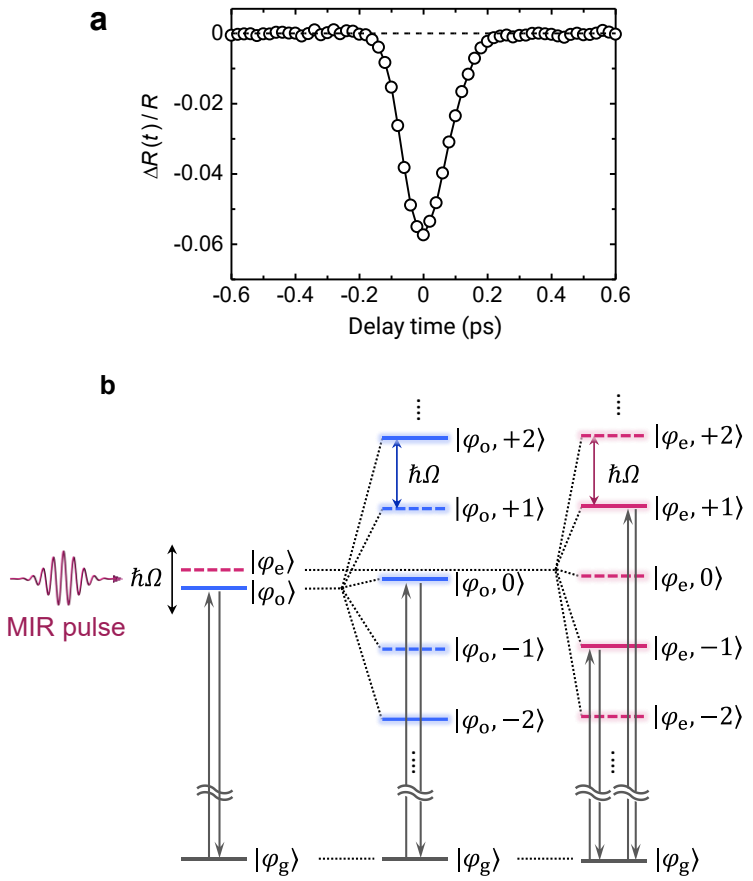

Fig. S2 | Coherent responses associated with excitonic Floquet states under MIR electric fields. a, The time characteristic of $-\Delta R/R(t)$ for the amplitude of the MIR pump pulse, $|E_{\mathrm{MIR}}| = 3.0$ MV/cm, extracted from Fig. 3d in Sr_2CuO_3 in the main paper. The photon energy $\hbar\Omega$ of the MIR pump light is 0.263 eV. The polarizations of the MIR pump and VIS probe lights are both parallel to the *b*-axis. **b,** Energy-level structures of the excitonic Floquet states and related optical processes in 1D Mott insulators. The left panel shows the original excitonic states $|\varphi_o\rangle$ and $|\varphi_e\rangle$. The middle and left panels show the excitonic Floquet states of the odd-parity exciton $|\varphi_o, m\rangle$ and even-parity exciton $|\varphi_e, m\rangle$, respectively, under an MIR electric field of frequency Ω. Vertical arrows indicate linear optical processes involving the incident and emitted light.

an oscillating electric field of frequency Ω, which is larger than the frequency difference between $|\varphi_o\rangle$ and $|\varphi_e\rangle$, is applied to this state, $|\varphi_o\rangle$ and $|\varphi_e\rangle$ are converted to $|\varphi_o, 0\rangle$ and $|\varphi_e, 0\rangle$, respectively, and move slightly closer together[5]. Furthermore, the sidebands $|\varphi_o, \pm m\rangle$ and $|\varphi_e, \pm m\rangle$ are created at a frequency $(\pm m\Omega)$ apart from $|\varphi_o, 0\rangle$ and $|\varphi_e, 0\rangle$, respectively (the right part of Fig. S2(b)), where m is a natural number. This

state under an oscillating electric field is generally called the Floquet state[6-8]. In this situation, $|\varphi_o, 0\rangle$, $|\varphi_o, \pm 2m\rangle$, and $|\varphi_e, \pm(2m-1)\rangle$ are one-photon allowed states. Considering only third-order optical nonlinearity, the oscillator strength of the transition from the ground state $|\varphi_g\rangle$ to $|\varphi_o\rangle$ without an MIR electric field is transferred not only to the $|\varphi_g\rangle \rightarrow |\varphi_o, 0\rangle$ transition but also to the $|\varphi_g\rangle \rightarrow |\varphi_e, \pm 1\rangle$ transitions under an MIR electric field[5]. As a result, the reflectivity around the peak corresponding to the $|\varphi_g\rangle$ to $|\varphi_o\rangle$ transition decreases. Such excitonic Floquet state formation is a type of coherent response that occurs only when the MIR pulse is irradiating[5,9-11], resulting in a pulsed signal reflecting its coherent nature, as shown in Fig. S2(a).

Therefore, the time characteristic of $-\Delta R/R(t)$ shown in Fig. S2(a) should be proportional to the convolution integral of the intensity profiles of the MIR pump pulse and visible probe pulse. In addition, as described in Section S3, the observed $-\Delta R/R(t)$ signal exhibits a Gaussian shape centred at the time origin. In this case, the temporal width t_S (FWHM) of this coherent response, $-\Delta R/R(t)$, can be expressed using the temporal widths t_{MIR} and t_{VIS} (FWHM) of the MIR pump pulse and visible probe pulse, respectively, as follows:

$$t_S = ({t_{MIR}}^2 + {t_{VIS}}^2)^{\frac{1}{2}} \quad \text{(S1)}$$

The t_{VIS} of the probe pulse was ~55 fs, whereas the t_S of the reflectivity-change signal (Fig. 3d and Fig. S2(a)) at $|E_{MIR}| = 3.0$ MV/cm was ~180 fs. From these values, the t_{MIR} of the MIR pulse used for PPR measurements was estimated to be ~170 fs. Using the same method, the t_{MIR} of the MIR pulse used for HHG measurements was estimated to be ~220 fs.

The maximum electric-field amplitude $|E_{MIR}|$ of an MIR pulse in each measurement was calculated from the photon energy $\hbar\Omega$, temporal width t_{MIR}, fluence F_s of the MIR pulse, and spot size l_s (FWHM) at the sample position of the MIR pulse. In the PPR and HHG measurements, $l_s = 45$ and 32.5 μm, respectively, and the maximum powers of the MIR pulses are 1.51 and 0.79 μJ, respectively, from which the $|E_{MIR}|$ values are estimated to be 13.7 and 12.3 MV/cm, respectively. The spot size of the probe pulse in PPR measurements (23.6 μm) was sufficiently small compared with that of the pump pulse (45 μm).

S2 Polarisation dependence of HH spectra

Figures S3(a–c) shows the HH spectra with the light polarisation E_r parallel and perpendicular to the b-axis ($E_r // b$ and $E_r \perp b$, respectively) in Sr_2CuO_3 on excitation with an MIR pulse (0.263 eV and $|E_{MIR}| = 12.3$ MV/cm) with the light polarisation E_{ex} parallel or perpendicular to the b-axis ($E_{ex} // b$ or $E_{ex} \perp b$, respectively). When the HH intensity for $E_{ex} // b$ and $E_r // b$ is expressed as I_{pp}, that for $E_{ex} // b$ and $E_r \perp b$, I_{ps}, is roughly equal to $10^{-2} I_{pp}$, and that for $E_{ex} \perp b$ and $E_r // b$, I_{sp}, is smaller than $10^{-2} I_{pp}$, except for the 3rd order harmonic. The HH intensity for $E_{ex} \perp b$ and $E_r \perp b$, I_{ss}, is smaller than I_{ps} and I_{sp} (not shown). These results are consistent with the strong one-dimensionality of the electronic state of Sr_2CuO_3.

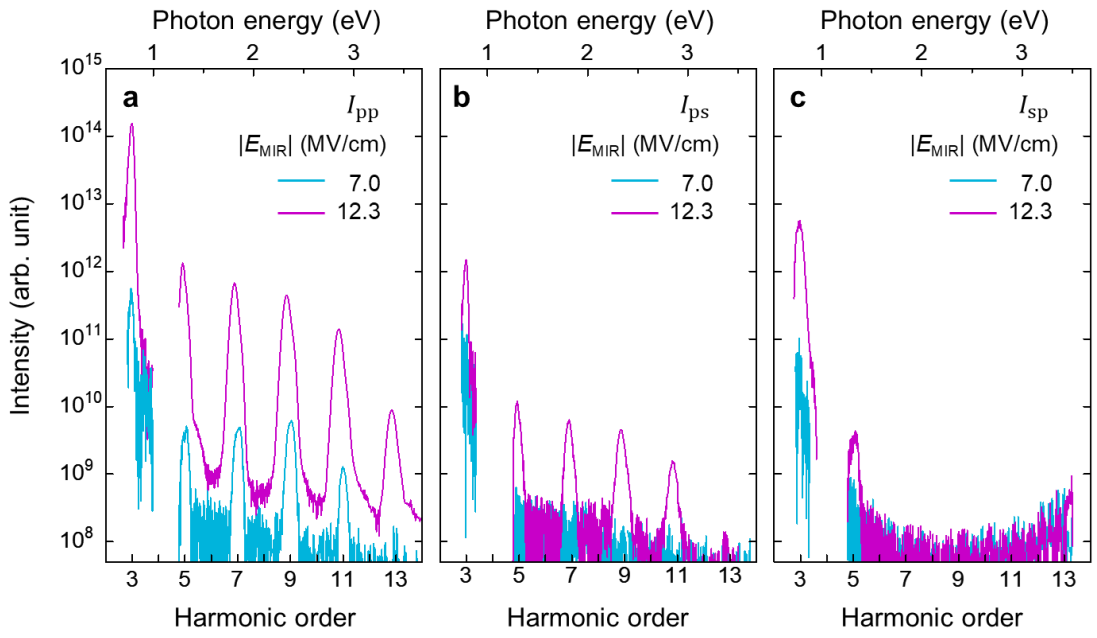

Fig. S3 | Polarization dependence of HH spectra in Sr_2CuO_3. The photon energy $\hbar\Omega$ is 0.263 eV, and the electric field amplitude $|E_{MIR}|$ is 12.3 or 7.0 MV/cm. (**a**) I_{pp}: $E_{ex} // b$ and $E_r // b$, (**b**) I_{ps}: $E_{ex} // b$ and $E_r \perp b$, and (**c**) I_{sp}: $E_{ex} \perp b$ and $E_r // b$. E_{ex} and E_r are the polarization of the MIR pump and HH light, respectively.

S3 Fitting analysis of transient reflectivity changes induced by MIR pump pulses

In this section, we discuss the analysis of the time characteristics of the reflectivity changes $\Delta R(t)/R$ induced by an MIR pulse (shown in Fig. 3d of the main text). Figures

S4(a), (b), and (c, d) show the time characteristics of $\Delta R(t)/R$ for the MIR pulse with $|E_{\mathrm{MIR}}|$ =3.0, 7.0, and 12.0 MV/cm. As described in Section S1, in the $\Delta R(t)/R$ signal induced by the MIR pulse with $|E_{\mathrm{MIR}}|$ =3.0 MV/cm, only the coherent response due to the 3rd order optical nonlinearity appears. This signal can be fitted with the following Gaussian-type function, as indicated by the light blue line in Fig. S4(a):

$$\frac{\Delta R(t)}{R} = -A_0 \exp\left[-\left(\frac{t}{\tau_0}\right)^2\right] \tag{S2}$$

τ_0 is 108 fs, which corresponds to t_S~180 fs, as mentioned in Section S1.

As described in the main text, at $|E_{\mathrm{MIR}}|$ =7.0 and 12.0 MV/cm, a component with a finite decay time due to generated carriers appears in the $\Delta R(t)/R$ signals. When carriers are annihilated by recombination, the signals due to the increase in temperature are superimposed. According to a previous study, the reflectivity at 1.79 eV, where $\Delta R(t)/R$ is measured, decreases with increasing temperature[2]. Following the previously reported analysis of photoinduced transient reflectivity changes in Mott insulators, we assume that the time characteristic of the carrier recombination is expressed as an exponential function with a decay time of τ_1; the time characteristics of the increase in temperature are expressed by a term including two exponential functions representing its rise and decay[12]. The rise and decay time are τ_1 and τ_2, respectively. In this case, $\Delta R(t)/R$ can be expressed as follows:

$$\frac{\Delta R(t)}{R} = -A_0 \exp\left[-\left(\frac{t}{\tau_0}\right)^2\right] - \int_{-\infty}^{t} A_1 \exp\left(-\frac{t-t'}{\tau_1}\right) \frac{1}{\sqrt{\pi}\tau_0} \exp\left[-\left(\frac{t'}{\tau_0}\right)^2\right] dt'$$

$$- \int_{-\infty}^{t} A_2 \left[1 - \exp\left(-\frac{t-t'}{\tau_1}\right)\right] \left[\exp\left(-\frac{t-t'}{\tau_2}\right)\right] \frac{1}{\sqrt{\pi}\tau_0} \exp\left[-\left(\frac{t'}{\tau_0}\right)^2\right] dt' \tag{S3}$$

The first term represents the coherent response ($\tau_0 = 0.108$ ps) expressed by equation (S2), the second term represents the reduction in reflectivity due to electric-field induced carriers that disappear with the decay time of τ_1, and the third term represents the reduction in reflectivity due to the increase in temperature with the rise time of τ_1 and decay time of τ_2. The time characteristics of $\Delta R(t)/R$ at $|E_{\mathrm{MIR}}| = 7.0$ and 12.0 MV/cm are well reproduced by this equation, as shown by the blue lines in Figs. S3(b–d). The three components represented by the first, second, and third terms are indicated by light blue, pink, and yellow lines, respectively. The parameters obtained from this

fitting analysis are listed in Table S1 along with the results for $|E_{\mathrm{MIR}}| = 3.0$ MV/cm. For $|E_{\mathrm{MIR}}| = 7.0$ and 12.0 MV/cm, τ_1 was 0.60 and 0.77 ps, respectively, and τ_2 was 150 ps. The magnitude of the coherent response, A_0, decreased considerably at $|E_{\mathrm{MIR}}| = 12.0$ MV/cm compared to that at $|E_{\mathrm{MIR}}| = 7.0$ MV/cm, likely owing to the disruption of coherence caused by carrier generation.

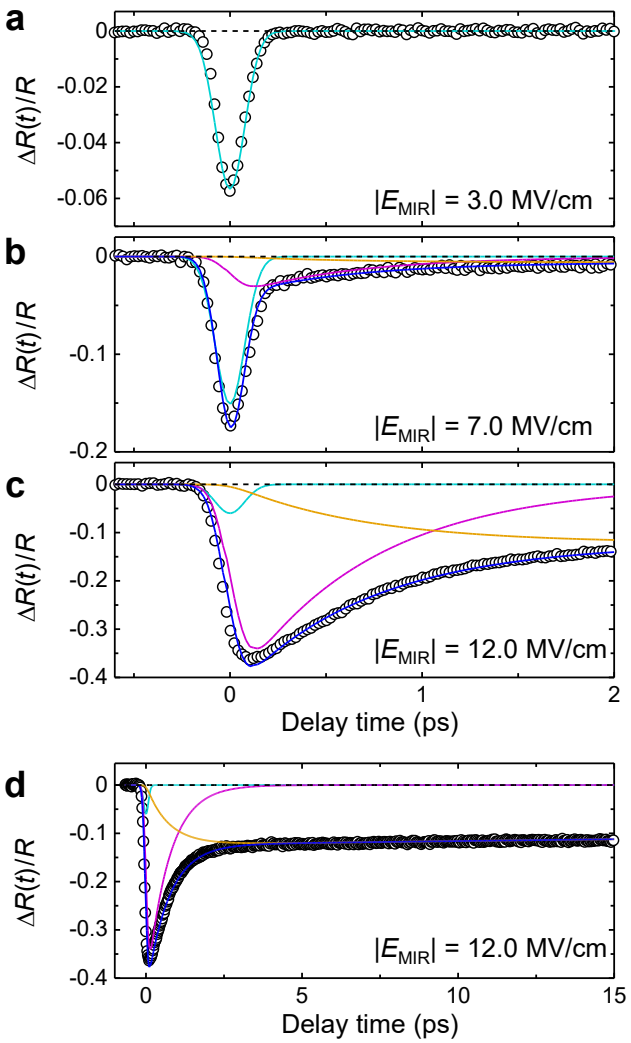

Fig. S4 | Analyses of the time characteristics of $-\Delta R(t)/R$ in Sr_2CuO_3. (**a**) $|E_{\mathrm{MIR}}| = 3.0$ MV/cm, (**b**) $|E_{\mathrm{MIR}}| = 7.0$ MV/cm, and (**c, d**) $|E_{\mathrm{MIR}}| = 12.0$ MV/cm. The photon energy of the MIR pump light, $\hbar\Omega$, is 0.264 eV. E_{ex} and E_{r} are both parallel to the *b*-axis. Data marked by open circles are extracted from Fig. 3d in the main text. Light-blue, pink, and yellow lines indicate the components of the first, second, and third terms in equation (S3). The blue lines in (**b–d**) indicate the sum of three components corresponding to the three terms in equation (S3).

Table S1 | Fitting parameters of $-\Delta R(t)/R$ in Sr_2CuO_3.

$\lvert E_{\mathrm{MIR}}\rvert$ (MV/cm)	3.0	7.0	12.0
A_0	0.033±0.002	0.092±0.004	0.035±0.05
τ_0 (ps)	0.108±0.005	0.108±0.005	0.108±0.005
A_1	0	0.04±0.004	0.43±0.014
τ_1 (ps)	–	0.6±0.05	0.7±0.03
A_2	0	0.006±0.0005	0.124±0.003
τ_2 (ps)	–	150±30	150±30

S4 Evaluation of the carrier density generated by MIR pump pulses

In this section, we discuss the procedure followed to estimate the carrier density n_{c} from the reflectivity change $\Delta R(t)/R$ mentioned in the previous section. The $-\Delta R(t)/R$ at $t = 0.25$ ps, $-\Delta R(0.25\ \mathrm{ps})/R$, when the coherent response completely disappears, is mainly attributable to generated carriers. Therefore, the magnitude of $-\Delta R(0.25\ \mathrm{ps})/R$ can be used to estimate n_{c}. More precisely, since $-\Delta R(0.25\ \mathrm{ps})/R$ includes the signal due to the temperature increase represented by the yellow line in Figs. S3(b–d), the net amount of carriers can be attributed to 0.91 of the $-\Delta R(0.25\ \mathrm{ps})/R$ signal for $\lvert E_{\mathrm{MIR}}\rvert$ =7.0 MV/cm and 0.9 of the $-\Delta R(0.25\ \mathrm{ps})/R$ signal for $\lvert E_{\mathrm{MIR}}\rvert =$ 12 MV/cm. Notably, it is reasonable to estimate the value of n_{c} from the maximum absolute value of $-\Delta R(t)/R$ represented by the pink line, which is 1.13 of $-\Delta R(0.25\ \mathrm{ps})/R$ for $\lvert E_{\mathrm{MIR}}\rvert$ =7.0 MV/cm and 1.13 of $-\Delta R(0.25\ \mathrm{ps})/R$ for $\lvert E_{\mathrm{MIR}}\rvert =$ 12 MV/cm. Since these corrections cancel out, it is reasonable to estimate n_{c} from the magnitude of $-\Delta R(0.25\ \mathrm{ps})/R$ itself.

Next, converting the magnitude of $-\Delta R(0.25\ \mathrm{ps})/R$ to the change in the imaginary part of the dielectric constant, ε_2, showing the absorption is necessary. The ε_2 spectrum near the Mott gap of Sr_2CuO_3 consists of two states: an excitonic state of a bound doublon–holon pair and a continuum starting just above the excitonic state[2]. Therefore, we first attempted to reproduce the steady state R and ε_2 spectra using two Lorentz oscillators corresponding to the excitonic state and continuum. In general, optical transition to a continuum cannot be expressed using a Lorentz oscillator. However, in our case, to consider the effect of the change in transition intensity on the reflectivity change, we simply adopted a Lorentz oscillator. The following complex dielectric function $\tilde{\varepsilon}(\omega)$ consisting of two Lorentz terms, LO1 and LO2, was used for analysis:

$$\tilde{\varepsilon}(\omega) = \varepsilon_\infty + \frac{S_1}{{\omega_1}^2 - \omega^2 - i\gamma_1\omega} + \frac{S_2}{{\omega_2}^2 - \omega^2 - i\gamma_2\omega} \tag{S4}$$

S_1 (S_2) is a parameter representing the transition intensity, ω_1 (ω_2) is the central frequency, γ_1 (γ_2) is the damping constant in the transition to excitons (continuum), and ε_∞ is the dielectric constant at high frequencies. The R and ε_2 spectra shown by the black solid lines in Fig. S5(a) and (b), respectively, are almost reproduced by $\tilde{\varepsilon}(\omega)$ in equation (S4), as indicated by broken purple lines in both figures. The ε_2 spectra of the two Lorentz components LO1 and LO2 are shown by blue and yellow solid lines, respectively, in Fig. S5(c). These results are presented in Fig. 3(b, c) in the main text, and these parameters are listed in Table S2.

Second, we assumed that the transition intensities of the two Lorentz components LO1 and LO2, I_{LO1} and I_{LO2}, in equation (S4) decrease at the same rate when doublons and holons are produced. Namely, $\Delta I_{\mathrm{LO1}}/I_{\mathrm{LO1}} = \Delta I_{\mathrm{LO2}}/I_{\mathrm{LO2}} = \Delta I/I$, where $I = I_{\mathrm{LO1}} + I_{\mathrm{LO2}}$ is the total transition intensity, and ΔI_{LO1}, ΔI_{LO2}, and ΔI are the changes in I_{LO1}, I_{LO2}, and I, respectively. For example, when $-\Delta I/I$ is set to 0.5, i.e., I is reduced to $0.5I$ ($= 0.5I_{\mathrm{LO1}} + 0.5I_{\mathrm{LO2}}$), R and ε_2 are reduced, the spectra of which are shown by the green broken lines in Fig. S5(a) and (b), respectively. The ε_2 spectra of the two Lorentz components, LO1 and LO2, are shown by the blue and yellow broken lines, respectively, in Fig. S5(c). The relationship between $-\Delta R(0.25\ \mathrm{ps})/R$ and $-\Delta I/I$ is analysed by changing $-\Delta I/I$, as shown in Fig. S5(d).

Finally, the value of $-\Delta I/I$ should be converted to n_{c}. Figures S5(e) and (f) show schematics of the electron configurations in the ground and excited states, respectively, where one doublon (D) and one holon (H) exist. When a D and H are generated by an MIR pulse, a Drude response is expected in the optical spectrum along with a reduction in the transition intensity near the Mott gap[13]. This reduction in transition intensity likely occurs because transitions beyond the Mott gap should not occur between a carrier-existing site and its two neighbouring sites (Fig. S5(e, f)). In this case, since one carrier eliminates the optical transitions for two sites, the relationship between the rate of reduction in the transition intensity near the Mott gap, $-\Delta I/I$, and n_{c} is likely described as $-\Delta I/I = 2n_{\mathrm{c}}$. Rigorous theoretical calculations showed that the transition intensity decreases with a slope slightly steeper than $-\Delta I/I = 2n_{\mathrm{c}}$ with increasing carrier number[14]. Assuming the simple relationship $-\Delta I/I = 2n_{\mathrm{c}}$, we can transform the relation between $-\Delta R(0.25\ \mathrm{ps})/R$ and $-\Delta I/I$ (the left vertical axis) into a relation

between $-\Delta R(0.25\ \mathrm{ps})/R$ and n_c using the right vertical axis. From the latter relationship, we obtained the $|E_{\mathrm{MIR}}|$ dependence of n_c shown in Fig. 4(g) in the main text.

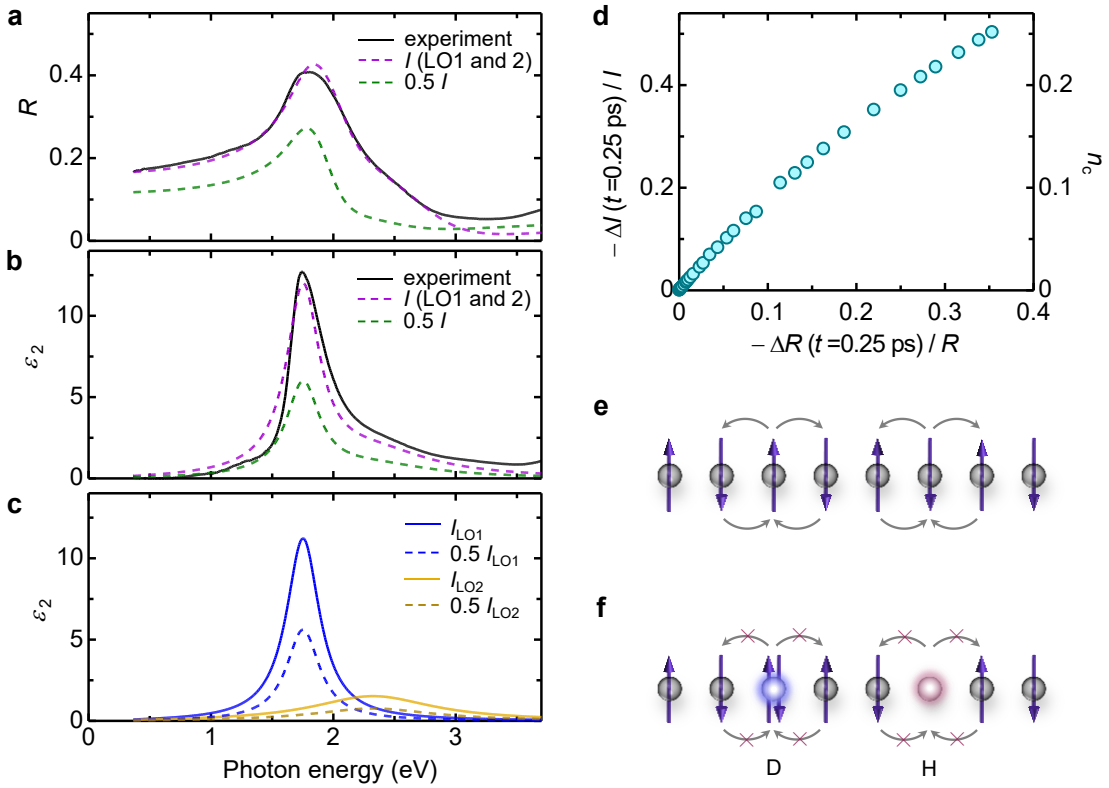

Fig. S5 | Estimation of the carrier density n_c generated by the MIR pulse in Sr_2CuO_3. a, Reflectivity (R) spectra. The black solid and purple broken lines show the experimental result and curve fitted with two Lorentz oscillators, respectively. The green broken line shows the simulation curve when the sum of intensities of the two Lorentz oscillators, I, is reduced to $0.5I$ $(-\Delta I(0.25\ \mathrm{ps})/I = 0.5)$. **b,** ε_2 spectra. The black solid and purple broken lines show the experimental result and curve fitted with two Lorentz oscillators, respectively. The green broken line shows the simulation curve for $0.5I$. **c,** The blue and yellow solid lines indicate the two Lorentz oscillator components I_{LO1} and I_{LO2} used for fitting curves of the steady state spectra shown by the purple broken lines in (**a, b**). The blue and yellow broken lines indicate the components of $0.5I_{\mathrm{LO1}}$ and $0.5I_{\mathrm{LO2}}$, respectively, in the simulation curves of the transient spectra marked by green broken lines in (**a, b**). **d,** The estimated dependence of $-\Delta I(0.25\ \mathrm{ps})/I$ and n_c on $-\Delta R(0.25\ \mathrm{ps})/R$. **e, f,** Schematics of a half-filled 1D Mott insulator state, (**e**) the ground state, and (**f**) an excited state with a doublon and holon.

Table S2 | Fitting parameters of R and ε_2 spectra for Sr_2CuO_3.

	$\hbar^2 S_{1,2}$ (eV^2)	$\hbar\omega_{1,2}$ (eV)	$\hbar\gamma_{1,2}$ (eV)	ε_∞
LO1	2.1±0.1	1.76±0.005	0.33±0.005	2.7±0.05
LO2	0.75±0.1	2.4±0.05	1.2±0.03	

S5 Supplementary data of DMFT simulations

This section presents supplementary data for the DMFT simulation of the single-band Hubbard model. The parameter sets for the system and pump pulse are the same as those mentioned in the main text, unless specified otherwise.

S5.1 Details of the HHG spectra

Figure S6 shows the HH spectra calculated using DMFT as a function of the field amplitude $|E_{\mathrm{MIR}}|$, which correspond to the experimental HH spectra shown in Fig. 2b and 4a–f in the main text. With increase in $|E_{\mathrm{MIR}}|$, the peak frequencies of the calculated nth harmonic spectra around $\omega = n\Omega$, $\omega_{\mathrm{peak},n}$, exhibit redshifts for $n > 5$, while they remain nearly unchanged for $n = 3$, consistent with the experimental observations. The behaviour of the peak for $n = 5$ represents an intermediate case.

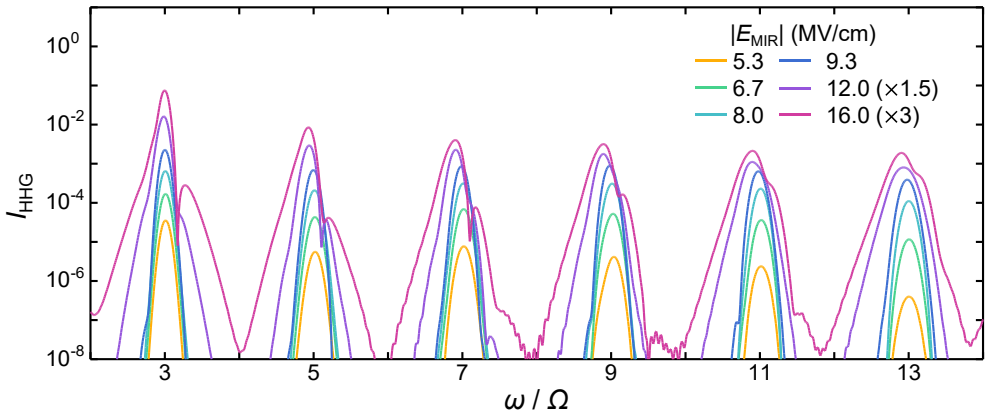

Fig. S6 | HH spectra calculated by DMFT. The parameter values of the model and pump pulse are described in the Method section in the main text.

Figure S7(a) shows the $|E_{\mathrm{MIR}}|$ dependence of the intensity of each harmonic, $I_{n\mathrm{HG}}$, which is evaluated by integrating $I_{\mathrm{HHG}}(\omega)$ around $\omega = n\Omega$. The overall trend is

consistent with the experimental results. Specifically, for $n = 3$, the $I_{3\mathrm{HG}}$ deviates upward from the scaling expected in the perturbation theory, $I_{3\mathrm{HG}} \propto |E_{\mathrm{MIR}}|^6$ (Fig. S7(b)). This enhancement can be attributed to a reduction in the Mott gap and an increase in the carrier density. The Mott-gap reduction enhances in-gap off-resonance processes, which dominate the third-harmonic generation in the perturbative regime, while the increase in carrier density enhances the contribution of intraband currents to the in-gap radiation. For $n = 5$, the intensity follows the perturbation theory as $I_{5\mathrm{HG}} \propto |E_{\mathrm{MIR}}|^{10}$ at low electric fields and then saturates. In contrast, for $n \geq 7$, the deviation from the perturbative scaling is downward, which appears even at low electric-field amplitudes (Fig. S7(b)). These trends are consistent with the experimental findings (Fig. 2c).

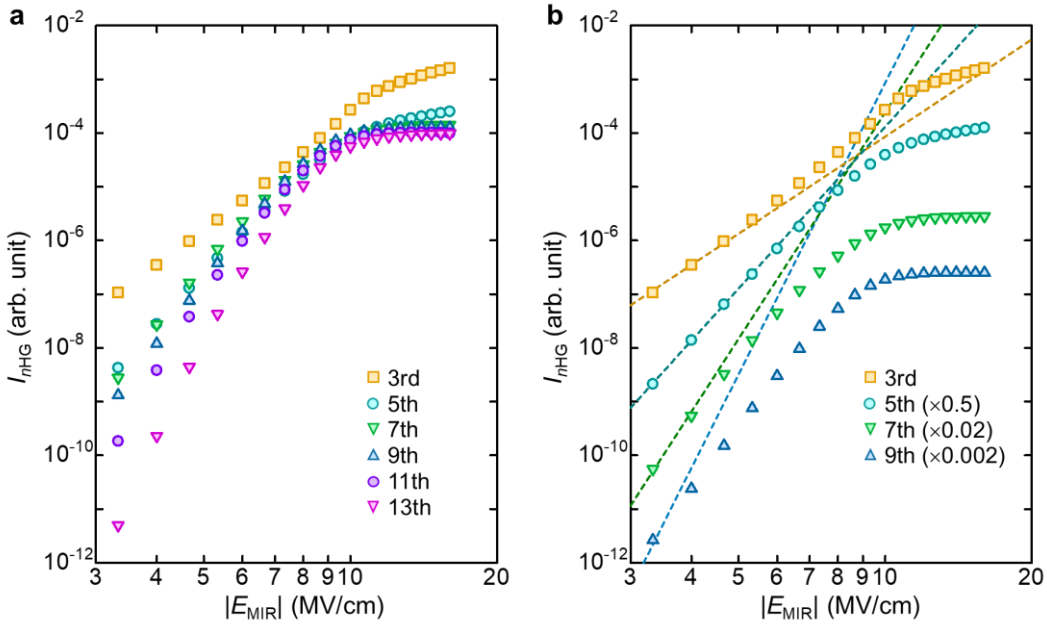

Fig. S7 | $|E_{\mathrm{MIR}}|$ dependence of the integrated intensities of HHs calculated by DMFT. a, Full data from the 3rd to 13th harmonics. **b,** Data from the 3rd to 9th harmonics multiplied by the factors shown in the panel. The broken lines show the relations expected from the perturbation theory ($I_{n\mathrm{HG}} \propto |E_{\mathrm{MIR}}|^{2n}$).

S5.2 Supplementary analyses for sub-cycle radiation

To extract the phases of sub-cycle radiations on a cycle-by-cycle basis, we applied a temporal window of half-cycle width $T_{\mathrm{hp}} = \pi/\Omega$ to the current. Specifically, we used the following window function:

$$F_{\mathrm{box}}(x,\eta)=\frac{1+\tanh\left(-\frac{2x-1}{2\eta}\right)\tanh\left(\frac{2x+1}{2\eta}\right)}{2}, \tag{S5}$$

which smoothly covers the range $x \in [-0.5, 0.5]$ with a smoothing width of η. To focus on the radiation around $t = t_{\mathrm{p}}$, we defined the sub-cycle current as follows:

$$J(t,t_{\mathrm{p}})=F_{\mathrm{box}}\left(\frac{t-t_{\mathrm{p}}}{T_{\mathrm{hp}}},\eta\right)J(t), \tag{S6}$$

which extracts the current around $t \in [\, t_{\mathrm{p}} - \frac{T_{\mathrm{hp}}}{2}, t_{\mathrm{p}} + \frac{T_{\mathrm{hp}}}{2}]$. When η is sufficiently small, the total current can be expressed as $J(t) = \sum_l J\left(t, t_{\mathrm{ref}} + lT_{\mathrm{hp}}\right)$, and similarly in the frequency domain as $J(\omega) = \sum_l J\left(\omega, t_{\mathrm{ref}} + lT_{\mathrm{hp}}\right)$, where t_{ref} is a constant that adjusts the central position within each time window. Constructive or destructive interference between the different sub-cycle radiations $J\left(\omega, t_{\mathrm{ref}} + lT_{\mathrm{hp}}\right)$ leads to peaks or valleys in $|J(\omega)|$ and in the corresponding HH spectrum $I_{\mathrm{HHG}}(\omega) = |\omega J(\omega)|^2$. We set $T_{\mathrm{hp}} =$ 7.6 fs ($\hbar\Omega = 0.263$ eV), $\eta = 0.2$, and $t_{\mathrm{ref}} = -1.59$ fs. In the range of $t \sim -$ 90 to 90 fs, 21 windows ($l = -10$ to 10) exist, as indicated by the coloured lines in Fig. S8, in which only windows with even numbers are shown. For these parameters, $\sum_l F_{\mathrm{box}}\left(\frac{t-t_{\mathrm{ref}}-lT_{\mathrm{hp}}}{T_{\mathrm{hp}}},\eta\right) \cong 1$, as shown by the grey solid line in the same figure.

In Fig. S9, the difference of $\mathrm{Arg}\left[J\left(\omega, t_{\mathrm{ref}} + lT_{\mathrm{hp}}\right)\right]$ from $\mathrm{Arg}\left[J\left(\omega, t_{\mathrm{ref}} + lT_{\mathrm{hp}}\right)\right]$ at $l = -9$, $\Delta\mathrm{Arg}[J(\omega,t)]$, at $\omega = n\Omega$ and $\omega = \omega_{\mathrm{peak},n}$ $(n = 3-11)$ for each half cycle are plotted. The $|E_{\mathrm{MIR}}|$ values are 6.7, 12.0, and 16.0 MV/cm. The marker size indicates the intensity of $\left|J\left(\omega, t_{\mathrm{ref}} + lT_{\mathrm{hp}}\right)\right|$. The data for the 3rd and 9th harmonics are shown in Figs. 5j–l in the main text. At $E_{\mathrm{MIR}} = 6.7$ MV/cm, the phase evolutions for $\omega = n\Omega$ and $\omega = \omega_{\mathrm{peak},n}$ are similar, and only slight differences appear in each cycle (see panels (a–e)). In contrast, at $E_{\mathrm{MIR}} = 12.0$ and 16.0 MV/cm, the phase difference remains small for $n = 3$, which corresponds to the in-gap radiation (see panels (f) and (k)). However, for higher harmonics ($n \geq 5$), a significant deviation arises between $\omega = n\Omega$ and $\omega = \omega_{\mathrm{peak},n}$; at $\omega = n\Omega$, finite phase variations occur depending on t, while at $\omega = \omega_{\mathrm{peak},n}$, phase variations are relatively small, particularly when the corresponding intensity is strong. This indicates that the radiation at $\omega = \omega_{\mathrm{peak},n}$

accumulates more constructively over cycles than that at the formal harmonic frequency $\omega = n\Omega$.

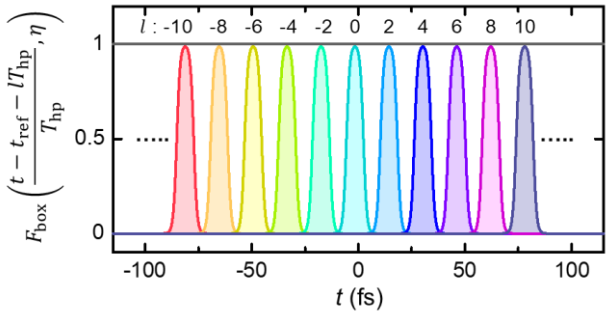

Fig. S8 | Window functions $F_{\mathrm{box}}\left(\frac{t-t_{\mathrm{ref}}-lT_{\mathrm{hp}}}{T_{\mathrm{hp}}},\eta\right)$ for different values of l. Here, $t_{\mathrm{ref}} = -1.59$ fs and $\eta = 0.2$. The grey line shows $F_{\mathrm{tot}} \equiv \sum_l F_{\mathrm{box}}\left(\frac{t-t_{\mathrm{ref}}-lT_{\mathrm{hp}}}{T_{\mathrm{hp}}},\eta\right)$, which is practically 1.

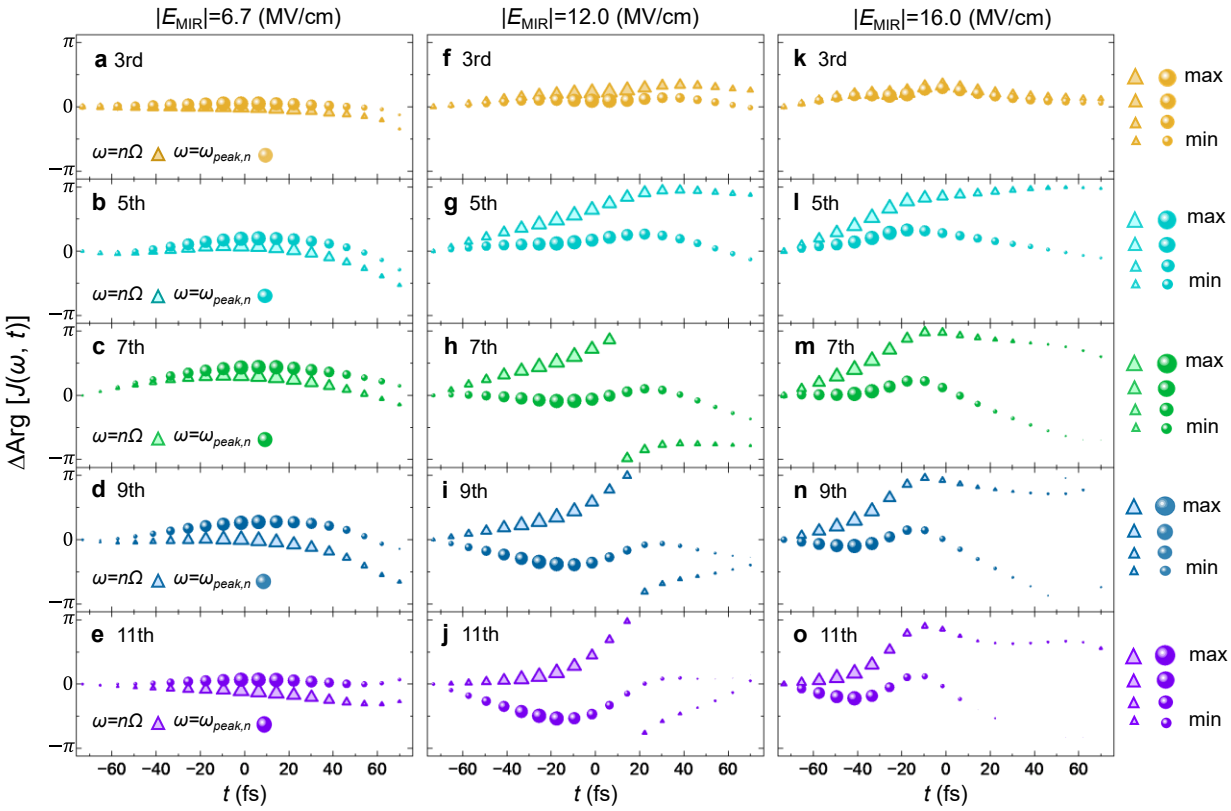

Fig. S9 | Phase changes for the 3rd to 11th harmonics, $\Delta\mathrm{Arg}[J(\omega,t)]$. The size of a marker is proportional to $|J(\omega,t)|$. (**a–e**) $|E_{\mathrm{MIR}}| = 6.7$ MV/cm, (**f–j**) $|E_{\mathrm{MIR}}| = 12.0$ MV/cm, and (**k–o**) $|E_{\mathrm{MIR}}| = 16.0$ MV/cm.

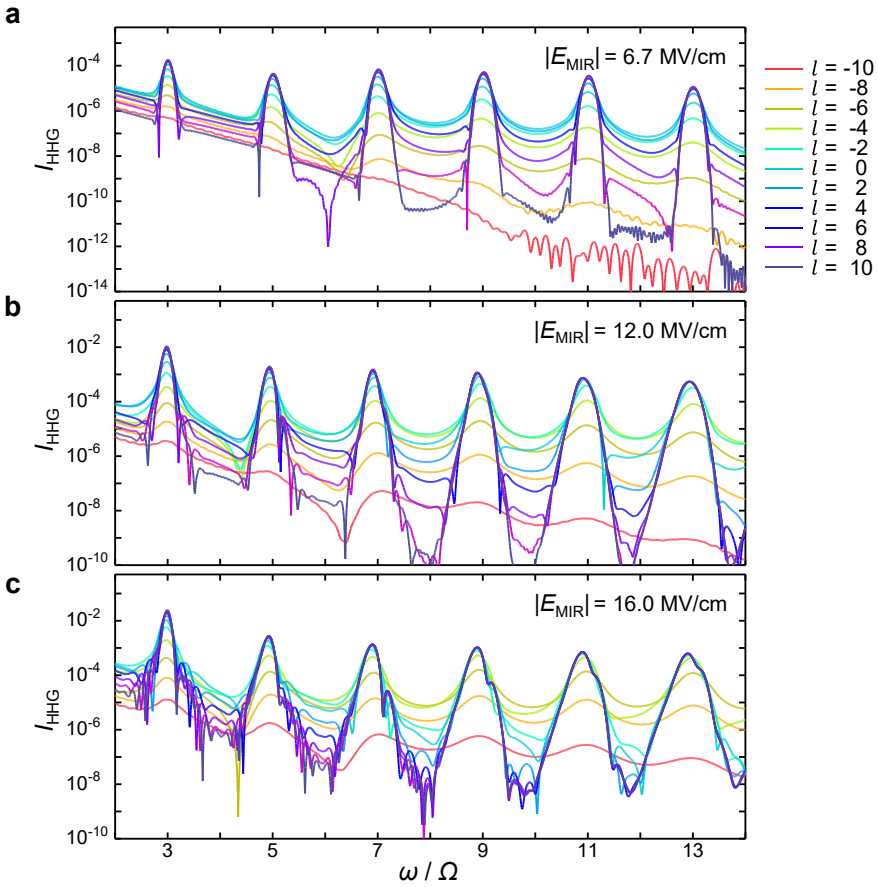

Fig. S10 | Truncated radiation spectra $\tilde{I}_l(\omega, t_{\mathrm{ref}})$ for different values of l. (**a**) $|E_{\mathrm{MIR}}| = 6.7\ \mathrm{MV/cm}$, (**b**) $|E_{\mathrm{MIR}}| = 12.0\ \mathrm{MV/cm}$, and (**c**) $|E_{\mathrm{MIR}}| = 16.0\ \mathrm{MV/cm}$. Each spectrum shows the radiation accumulated up to $t_{\mathrm{ref}} + lT_{\mathrm{hp}}$.

To investigate the cycle-by-cycle accumulation of HH intensity, the following truncated current was introduced:

$$\tilde{J}_l(t, t_{\mathrm{ref}}) = \sum_{k \le l} J\left(t, t_{\mathrm{ref}} + iT_{\mathrm{hp}}\right), \tag{S7}$$

which corresponds to the current accumulated up to $t = t_{\mathrm{ref}} + lT_{\mathrm{hp}}$. The corresponding radiation spectrum is given by $\tilde{I}_l(\omega, t_{\mathrm{ref}}) = \left|\omega \tilde{J}_l(\omega, t_{\mathrm{ref}})\right|^2$. The results for even l are shown in Fig. S10. This figure conceptually corresponds to the schematics shown in Fig. 1a in the main text. For small values of l, the peak structures in the spectrum are not well developed; clear peak structures emerge with increasing l. Peaks appear at $\omega = n\Omega$ (n: odd number) for $E_{\mathrm{MIR}} = 6.7\ \mathrm{MV/cm}$, whereas they develop at the lower frequencies

($\omega < n\Omega$) for $E_{\mathrm{MIR}} = 12.0$ and $16.0\ \mathrm{MV/cm}$. These observations are consistent with the above-mentioned discussion on the radiation phase shown in Fig. S9.

S5.3 Carrier envelope phase (CEP) dependence of the HH spectrum and antiferromagnetic (AFM) order

Figure S11 shows the dependence of the HH spectrum and AFM order m_{AFM} on the CEP of the MIR pump pulse. Here, the CEP values of the MIR electric field, ϕ_{CEP}, are varied in steps of $\pi/8$ over the range of $[-\pi, \pi]$. Neither quantity depends upon the CEP values. Therefore, unlike other HH shift phenomena previously observed in semiconductors and topological insulators[15,16], the HH peak redshifts discussed in this study are not sensitive to CEP.

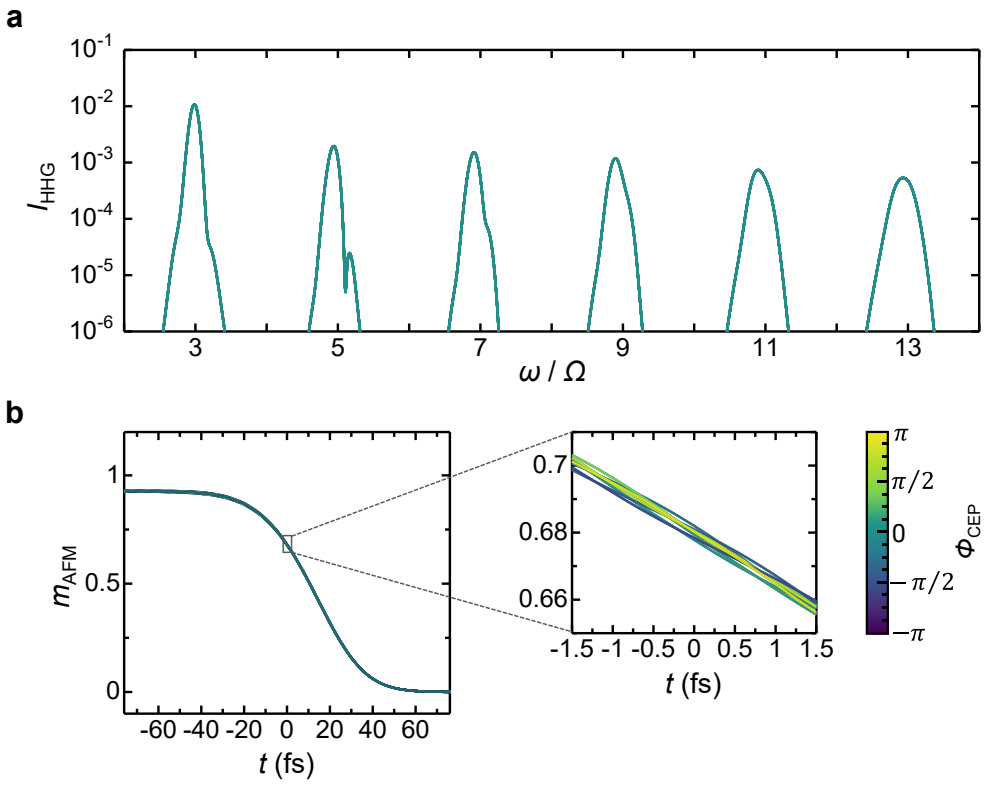

Fig. S11 | HH spectra and time dependence of the AFM order m_{AFM} for different values of CEP, ϕ_{CEP}, simulated by DMFT. $|E_{\mathrm{MIR}}| = 12.0\ \mathrm{MV/cm}$, and the ϕ_{CEP} is changed from $-\pi$ to π in steps of $\pi/8$. The results in (**a**) and (**b**) almost completely overlap with each other. In (**b**), a magnified view of the left panel is provided in the right panel to highlight the differences.

References

1. Kishida, H. et al. Gigantic optical nonlinearity in one-dimensional Mott–Hubbard insulators. *Nature* **405**, 929–932 (2000).
2. Ono, M. et al. Linear and nonlinear optical properties of one-dimensional Mott insulators consisting of Ni-halogen chain and CuO-chain compounds. *Phys*. *Rev*. *B* **70**, 085101 (2004).
3. Ono, M., Kishida, H., and Okamoto, H. Direct Observation of Excitons and a Continuum of One-Dimensional Mott Insulators: A Reflection-Type Third-Harmonic-Generation Studyof Ni-Halogen Chain Compounds. *Phys. Rev. Lett.* **95**, 087401 (2005).
4. Miyamoto, T. et al. Biexciton in one-dimensional Mott insulators. *Commun*. *Phys* **2**, 131 (2019).
5. Yamakawa, T. et al. Dynamical aspects of excitonic Floquet states generated by a phase-locked mid-infrared pulse in a one-dimensional Mott insulator. *New J*. *Phys*. **25**, 093044 (2023).
6. Oka, T. & Kitamura, S. Floquet Engineering of Quantum Materials. *Annu*. *Rev*. *Condens*. *Matter Phys*. **10**, 387 (2019).
7. Wang, Y. H. et al. Observation of Floquet-Bloch States on the Surface of a Topological Insulator. *Science* **342**, 453-457 (2013).
8. Merboldt, M. et al. Observation of Floquet states in graphene. *Nat*. *Phys*. (2025).
9. Ikeda, R. et al., Observation of excitonic Floquet states in a one-dimensional organic Mott insulator using mid-infrared pump near-infrared probe reflection spectroscopy. Preprint at https://arxiv.org/abs/2407.17759
10. Zhou, S. et al. Pseudospin-selective Floquet band engineering in black phosphorus., *Nature* **614**, 75-80 (2023).
11. Shan, J-Y. et al. Giant modulation of optical nonlinearity by Floquet engineering. *Nature* **600**, 235–239 (2021).
12. Okamoto, H. et al. Photoinduced transition from Mott insulator to metal in the undoped cuprates Nd_2CuO_4 and La_2CuO_4. *Phys. Rev. B* **83**, 125102 (2011).
13. Okamoto, H. et al. Photoinduced Metallic State Mediated by Spin-Charge Separation in a One-Dimensional Organic Mott Insulator. *Phys*. *Rev*. *Lett*. **98**, 037401 (2007).
14. Eskes, H. & Andrzej, M. O. Two Hubbard Bands: Weight Transfer in Optical and One-Particle Spectra. *Phys*. *Rev*. *Lett*. **73**, 1279 (1994).
15. Schubert, O. et al. Sub-cycle control of terahertz high-harmonic generation by dynamical Bloch oscillations. *Nat. Photon*. **8**, 119–123 (2014).

16. Schmid, C. P. et al. Tunable non-integer high-harmonic generation in a topological insulator. *Nature* **593**, 385–390 (2021).